

# Plasmon-Driven Selective Deposition of Au Bipyramidal Nanoparticles

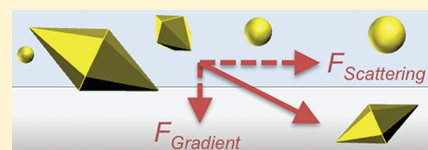
Mason J. Guffey,<sup>†</sup> Ryan L. Miller,<sup>‡</sup> Stephen K. Gray,<sup>‡</sup> and Norbert F. Scherer<sup>\*,†,‡</sup>

<sup>†</sup>Department of Chemistry and the James Franck Institute, The University of Chicago, 929 East 57th Street, Chicago, Illinois 60637, United States

<sup>‡</sup>Center for Nanoscale Materials, Argonne National Laboratory, Argonne, Illinois 60439, United States

**S** Supporting Information

**ABSTRACT:** We demonstrate the plasmon-selective and driven deposition of (bipyramidal) Au nanoparticles on transparent substrates (glass coverslips) utilizing total internal reflection (TIR) illumination. Near-IR laser light undergoing TIR at a glass–water interface causes colloidal Au bipyramids to irreversibly deposit onto the glass surface. We demonstrate that the deposition process has particle (i.e., shape) selectivity that is associated with resonant plasmon excitation. Specifically, the deposition is selective for the bipyramids over spheroidal particles that are also present in solution due to the former's surface plasmon resonance in the near-IR region. Our measurements, finite difference time domain simulations, and the results of an analytical model show that the optical (i.e., scattering and gradient) forces that act on the particles are large and cause the observed acceleration and directed motion of the bipyramids. These directional forces play a major role in the spatial pattern of particle deposition that is observed. In addition, the resonant photothermal heating of the Au bipyramids causes an irreversible loss in colloidal stability, thus allowing them to adhere to the surface. Structural (i.e., scanning electron microscopy) characterization of the deposited bipyramids reveals a slight reduction in aspect ratio relative to the ensemble, consistent with the proposed (heating) mechanism. To our knowledge this is the first demonstration of the plasmon-selective deposition of metal nanoparticles from a heterogeneous mixture.



**KEYWORDS:** Au, nanoparticle, bipyramid, optical trapping, evanescent field, total internal reflection, localized surface plasmon resonance, directed assembly

Metal nanoparticles (MNPs), particularly those consisting of Au or Ag, exhibit a collective oscillation of conduction electrons commonly described as a “plasmon resonance” at certain defined frequencies in the visible and near-infrared range of the optical spectrum.<sup>1</sup> The unique characteristics of plasmon resonances in MNPs include both greatly enhanced optical extinction cross sections relative to their geometric cross sections and concentration of electromagnetic energy near the MNP surface.<sup>2</sup> Most of the proposed applications of MNPs in biosensing,<sup>3</sup> optoelectronics,<sup>4</sup> and solar cells<sup>5</sup> take advantage of these plasmonic phenomena. In particular, bipyramidal Au nanoparticles (Au bipyramids), owing to their narrow (ensemble) plasmon line width (with relatively little inhomogeneous broadening) and strong field concentration at their tips, show great promise as label-free biosensors.<sup>6–8</sup>

Methods for positioning MNPs on surfaces in a controlled manner would enhance the study of their fundamental properties such as field enhancement, electromagnetic coupling,<sup>9</sup> and quantum effects,<sup>10</sup> as well as provide pathways for practical applications. Currently, one is faced with a trade-off between obtaining positional precision and fidelity of plasmonic properties. Although e-beam lithography allows a high degree of control over MNP positioning,<sup>11</sup> grain boundaries and surface defects in MNPs formed by physical vapor deposition can result in greater plasmon damping relative to analogous colloidal MNPs.<sup>12–14</sup> On the other hand, applications using colloiddally synthesized MNPs that are crystalline require solving the nontrivial challenge of their deposition from solution into ordered arrangements on surfaces.

Self-assembly can be used to create long-range ordered two-<sup>15–17</sup> and three-dimensional<sup>18</sup> superlattice arrays of colloidal nanoparticles with impressive quality. However, self-assembly methods are generally not suited for positioning MNPs at arbitrary locations or in specific arrangements on surfaces. The latter requires “directed assembly”.<sup>19</sup> Several directed assembly methods that are compatible with colloidal metal nanoparticles have been developed.<sup>20</sup> These techniques include (i) the fabrication of surface features such as pits and trenches using e-beam lithography,<sup>21,22</sup> (ii) various schemes that utilize electrostatic and dielectrophoretic forces,<sup>23–25</sup> and (iii) scanning probe-based methods such as dip-pen nanolithography.<sup>26,27</sup> Furthermore, selectively depositing MNPs with a specific plasmon resonance out of a heterogeneous mixture remains a challenge for most directed assembly methods.

The manipulation of MNPs by optical forces offers a possible solution to this challenge in that a laser can selectively excite MNPs when tuned to their plasmon resonance. The optical manipulation of MNPs began with the pioneering work of Svoboda et al. that demonstrated the three-dimensional optical trapping of 36 nm diameter Au particles with a focused laser beam.<sup>28</sup> Since then, the types of plasmonic nanomaterials that can be optically manipulated with a focused laser beam has increased significantly to include a large range of sizes of spherical Au<sup>29</sup> and Ag nanoparticles,<sup>30</sup> Au<sup>31,32</sup> and

**Received:** March 27, 2011

**Revised:** August 21, 2011

**Published:** September 08, 2011

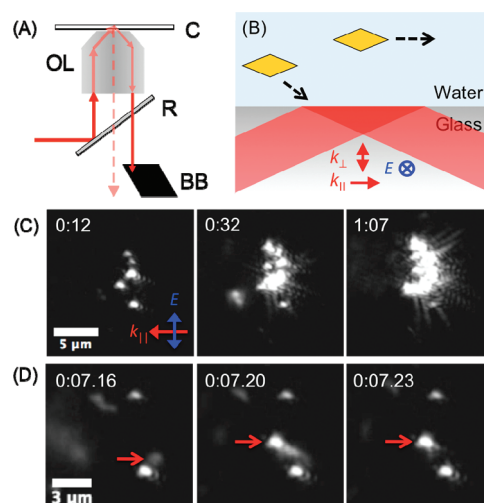
Ag nanoparticle aggregates,<sup>33</sup> Au nanorods<sup>34,35</sup> and bipyramids,<sup>36</sup> and Ag nanowires.<sup>37</sup> Recently, we reported the directed assembly of arrays of Au nanoparticles using optical traps and demonstrated  $\sim 100$  nm open-loop precision of positioning.<sup>38</sup>

In addition, it would be useful to have a multiplex assembly method that would complement the aforementioned serial manipulation approach. Evanescent optical fields that occur at interfaces have been shown to be capable of imparting force on MNPs, primarily in the form of one-dimensional propulsion along the propagation direction of the optical field.<sup>39–43</sup> Resonant excitation of plasmonic materials, including MNPs, results in enhanced electromagnetic fields at their surface(s). It is this field enhancement that can lead to local nonlinear processes at the surface of the MNP such as surface-enhanced Raman scattering (SERS),<sup>44</sup> second harmonic generation (SHG),<sup>45,46</sup> and two-photon fluorescence.<sup>47</sup> The enhancement can also give rise to electrodynamic interaction forces with other nearby particles.<sup>48,49</sup> As a result, plasmonic nanostructures can be used to trap colloidal dielectric objects.<sup>50–52</sup> However, the use of evanescent fields at a simple (unpatterned) dielectric interface (i.e., without any metal coating) to trap colloidal MNPs has not been demonstrated.

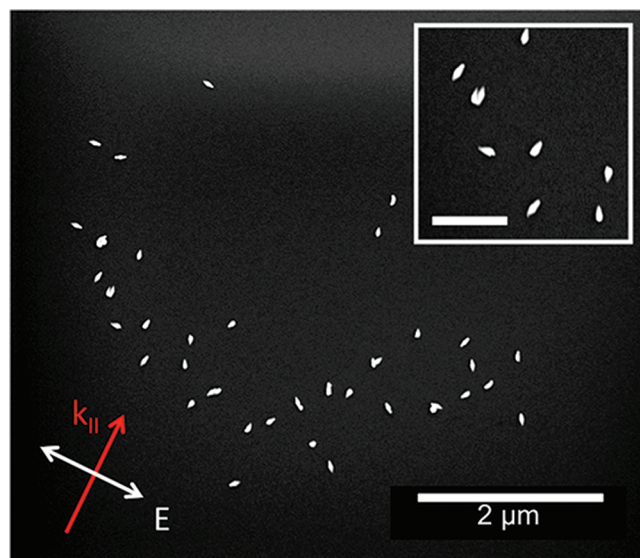
In this paper we demonstrate the plasmon-selective trapping of bipyramidal Au nanoparticles directly onto dielectric surfaces using an evanescent optical field created by total internal reflection (TIR) at a glass–water interface. Au bipyramids irreversibly deposit on glass coverslips as a result of the evanescent optical field from a near-infrared (NIR) laser beam that is resonant with the longitudinal plasmon mode of the Au bipyramids. The resonant interaction enhances the gradient force and hence the probability of particle collision with the surface. Concomitantly, the associated heating destabilizes the ligand coating on the particle allowing adhesion to the surface. As a result, the process is highly selective for the NIR-resonant bipyramids versus spheroidal Au nanoparticles that are also present in solution. To our knowledge this is the first observation of the plasmon-selective deposition of MNPs from a heterogeneous mixture.

Figure 1A depicts the experimental setup (see Methods section for details). Au bipyramids are observed to deposit on glass coverslips upon exposure to the NIR laser beam undergoing TIR. Blocking the reflected beam (see Figure 1A) creates a dark-field condition, allowing the light scattering from the nanoparticles to be observed on a CCD camera in real time as they deposit (see Figure 1C, and movie file in Supporting Information). The nanoparticles are observed to deposit in a crescent pattern on the coverslip surface only while exposed to the trapping laser. The nanoparticles appear to deposit in a sequential manner, as illustrated by three successive frames from a video (30 Hz frame rate) that are shown in Figure 1D. During the deposition process, Au nanoparticles are observed to rapidly stream through and often away from the illuminated area in the direction of the laser beam's propagation. This motion is highly directional (i.e., like short meteoric streaks). As discussed below in conjunction with the FDTD simulations and results from an analytical model, the directional motion results from the momentum imparted to the nanoparticles from the evanescent laser light.<sup>43</sup>

Depending on the deposition conditions (i.e., power and wavelength of the trapping laser), after  $\sim 30$  s a portion of the illuminated area becomes coated with Au nanoparticles (see Figure 1C). Due to both the subdiffraction-limited size of the deposited nanoparticles and their high density on the surface, we find that an ex situ measurement with nanoscale resolution



**Figure 1.** (A) Schematic of the total internal reflection (TIR) setup: C, coverslip; OL, 100 $\times$  oil immersion objective lens (Olympus, UPLSAPO); R, inconel-coated reflective neutral density filter; BB, beam block. (B) Cartoon depicting observed particle trajectories; some particles deposit on the surface toward the edge of the evanescent field area, while others stream past. (C) Dark-field optical images of bipyramid deposition at different times after the start of laser exposure (denoted as minutes:seconds). The laser propagation direction parallel and perpendicular to the surface,  $k_{\parallel}$  and  $k_{\perp}$ , and electric field polarization direction  $E$  are indicated on the figure. (D) Three successive frames (taken at 30 frames per second) showing a nanoparticle (highlighted with red arrow) accelerating toward the surface and depositing. Time is denoted on figure as minutes:seconds.centiseconds.



**Figure 2.** SEM image of Au bipyramids deposited by TIR. Laser propagation direction parallel to the surface  $k_{\parallel}$  and electric field polarization direction  $E$  are denoted. Inset: Detail of a portion of the image, scale bar is 500 nm.

(versus analysis of the optical image with its striking interference patterns) is necessary in order to determine the spatial and orientational characteristics of the particles deposited. Therefore, after a given amount of TIR laser exposure time (e.g., 10–30 s), the sample is removed from the optical microscope, cleaned,

sputtered with a thin layer of Pt/Pd, and imaged by scanning electron microscopy (SEM, see Methods). Figure 2 shows an SEM image of a typical result of particles deposited by TIR trapping on a glass surface, with the directions of the propagation vector  $k$  and the electric field vector  $E$  denoted. Actually, the density of particles shown in Figure 2 gives rise to an optical dark field image similar to that shown in Figure 1C. As observed during the optical trapping experiment, the particles deposit in a crescent pattern near the perimeter of the laser illumination (and evanescent field). Moreover, the crescent forms at the leading edge of the illumination spot (see Figure 1B); i.e., most particles appear to deposit as soon as they enter the illumination region, as shown in Figure 1D.

Au bipyramids were suspended in deuterium oxide ( $D_2O$ ) to test the possibility of direct laser heating of the solvent (water). At near-IR wavelengths,  $D_2O$  has an absorbance of  $\sim 0.004 \text{ cm}^{-1}$  compared to  $0.03 \text{ cm}^{-1}$  for water.<sup>53,54</sup> Thus, any direct optical heating of the solvent will be suppressed by an order of magnitude in  $D_2O$  compared to  $H_2O$ . However, Au bipyramids suspended in  $D_2O$  yield qualitatively similar results in terms of the observed crescent deposition pattern, the magnitude and wavelength dependence of the nanoparticle deposition rate, and the selectivity toward bipyramids over spheres (see Figure S1, Supporting Information), suggesting that direct solvent heating is not a significant factor in the deposition process. Moreover, the similar (crescent) deposition patterns observed when trapping particles suspended in  $H_2O$  and  $D_2O$  imply that this pattern is not a result of thermal convection.

An important result is the absence of deposition of spheroidal Au particles on the glass surfaces. Although the chemical synthesis of Au bipyramids produces a mixture of bipyramids and spheroidal shapes in roughly equal proportion,<sup>55</sup> the deposition is exclusively of Au bipyramids; i.e. no single spheroidal particles were observed! Figure 3A shows that the relative deposition rate of bipyramids depends strongly on the laser detuning from the ensemble bipyramid extinction peak. The marked dependence on the excitation wavelength demonstrates that the resonant optical excitation of the bipyramid plasmon is necessary for the deposition to occur.

The laser-power-dependent deposition rate,  $R(P)$ , as well as the number of particles deposited measured as a function of laser illumination time,  $N(t)$ , are plotted in panels B and C of Figure 3, respectively. The power densities represented in Figure 3B range from  $3.9$  to  $10.8 \times 10^5 \text{ W cm}^{-2}$  (see Methods section). Both  $R(P)$  (Figure 3B) and  $N(t)$  (Figure 3C) exhibit a linear dependence on the power and exposure time, respectively. In the case of  $R(P)$ , a threshold value of  $\sim 40 \text{ mW}$  total power is necessary to induce Au bipyramid deposition (this will be discussed below). That is, the repulsive electrostatic interactions of the surface coating and the CTAB on the bipyramids are sufficiently large that random thermal motion and energy ( $1/2 k_B T$ ) is insufficient to bring them to the surface and have them adhere.

Figure 4 displays the dependence of the size of the bipyramid deposition pattern on the total laser power. At lower powers (40 and 60 mW), the bipyramids deposit near the center of the region of laser illumination (i.e., where the evanescent field is most intense), while at higher powers (80–100 mW) the deposition occurs at larger distances from the center of the illuminated area. For the experimental conditions studied, the particles are never observed to deposit outside of the evanescent field area on the glass coverslip.

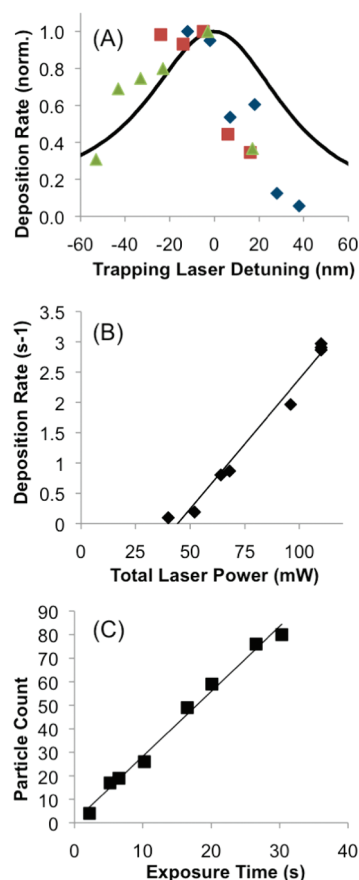


**Figure 3.** (A) Normalized deposition rates for three different Au bipyramid samples (symbols) as a function of laser detuning from the bipyramid longitudinal plasmon peak (un-normalized deposition rates vary from  $0.2$  to  $3.8 \text{ particles s}^{-1}$ ). The solid line is a typical Au bipyramid ensemble extinction spectrum. (B) Au bipyramid deposition rate measured as a function of power,  $R(P)$ , at a trapping laser wavelength of  $817 \text{ nm}$  ( $+20 \text{ nm}$  detuning from the ensemble bipyramid plasmon peak). (C) Number of nanoparticles deposited as a function of time,  $N(t)$ , at a total laser power of  $110 \text{ mW}$ . Solid lines are linear fits to the data, with correlation coefficients  $R^2 = 0.98$  for  $R(P)$ , and  $R^2 = 0.99$  for  $N(t)$ .

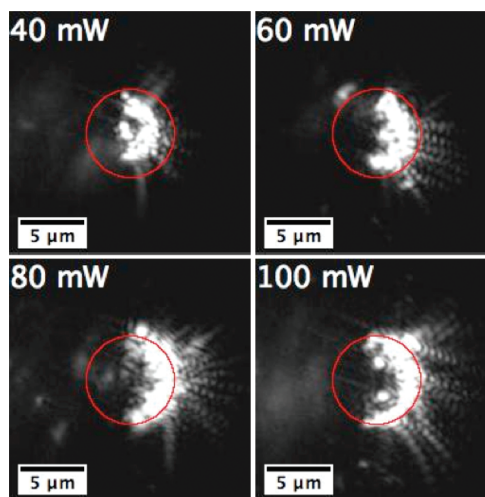


**Figure 4.** Optical images of laser scattering from Au bipyramids deposited at several optical power levels. Red circle indicates the location of the evanescent field determined independently (see Methods).

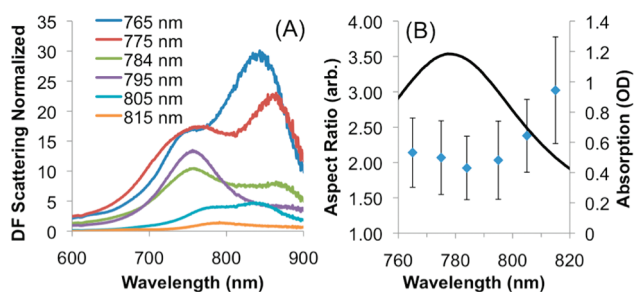


**Figure 5.** (A) Dark-field scattering spectra collected from Au bipyramids deposited at different trapping laser wavelengths. (B) Symbols: Aspect ratio of Au bipyramids deposited at different trapping laser wavelengths derived from SEM imaging (error bars are standard deviations). Solid line: Ensemble extinction spectrum of Au bipyramid sample.

By spatially correlating SEM imaging with dark-field imaging and spectroscopy,<sup>45,46</sup> we find that the bipyramids deposited by TIR have reduced aspect ratios and blue-shifted scattering spectra relative to the original ensemble. Figure 5A shows dark-field scattering spectra of bipyramids deposited at trapping laser wavelengths on either side of the bipyramid plasmon peak. The SEM images of the sample reveal that each deposited spot consists of  $\sim 10$ – $100$  bipyramids, depending on the detuning of the trapping laser from the bipyramid plasmon peak. The variation in the number of deposited particles reflects the changes in the deposition rate as a function of laser detuning from the bipyramid plasmon peak (see Figure 3A).

The dark-field spectra in Figure 5A show a blue-shifted resonance relative to the bipyramid ensemble plasmon resonance peak (plotted in Figure 5B). The blue-shifted peak could occur by photothermal annealing of the bipyramids that results in a lower aspect ratio. There is also a red-shifted scattering peak at wavelengths longer than 800 nm that is particularly pronounced for trapping laser wavelengths of 765 and 775 nm. This peak has been observed in previous measurements of dark-field scattering from Au bipyramids.<sup>6</sup> In the present case, the red-shifted peak is caused by chevron-shaped bipyramid dimers<sup>49</sup> observed to be present among the deposited bipyramids (see inset to Figure 2). On the basis of the comparison of the scattering spectra in Figure 5A with the ensemble spectrum in Figure 5B, we believe that these dimers form during trapping and deposition, since it is clear that their concentration on the surface is significantly enhanced relative to the ensemble.

The ensemble spectrum of the bipyramid sample is shown in Figure 5B, along with the average aspect ratio of the deposited bipyramids obtained via SEM imaging of the same sample. For trapping laser wavelengths close to the ensemble plasmon extinction peak, specifically 765–795 nm, the average aspect ratio of the deposited bipyramids shows a marked reduction to  $\sim 2$  from 2.5 to 3.0. This structural rearrangement is reflected in the dark-field scattering spectra in Figure 5A, which show a blue-shift for the bipyramids with the reduced aspect ratio. The data of this and the previous two paragraphs suggest that photothermal annealing of the Au bipyramids is occurring and this is a step in the proposed mechanism of deposition discussed below.

The observation of directional nanoparticle motion in our system has parallels to the phenomenon of light-induced drift, in which a chamber filled with an atomic or molecular gas will exhibit a measurable pressure difference due to momentum transfer from a laser to the absorbing species.<sup>56</sup> However, compared

to molecules in the gas phase, the Au bipyramids will experience a significantly enhanced viscous (Stokes) drag force.

Assuming that the nanoparticle (NP) can be approximated as an equivalent volume sphere, the drag force equal and opposite to the optical force will be  $F = 6\pi\eta Rv$ , where  $\eta$  is the dynamic viscosity of water,  $R$  is the radius of the equivalent volume sphere (15 nm), and  $v$  is the velocity of the particle. An estimation of the viscous drag force acting on the Au nanoparticles can be obtained by analyzing the particles' motion as captured by video (see movie file, Supporting Information). Analysis of six particle trajectories near the beginning of the video reveals a viscous drag force of  $6.4 \pm 3.7$  fN (mean plus or minus standard deviation). However, it should be noted that most particles that deposit simply appear and thus are moving faster than the camera's inverse frame rate (i.e.,  $30 \text{ frame s}^{-1}$ ; see Figure 1D), implying that some particles experience a significantly enhanced optical force relative to others. Nonetheless, assuming that the analyzed particles were experiencing a smaller force relative to most of the other particles under the influence of the TIR field, it can be concluded that the opposing (optical) force must be  $\geq 6$  fN in magnitude.

In order to obtain an idea of the optical forces acting on the bipyramids, we carry out three-dimensional finite-difference time-domain (FDTD)<sup>57</sup> electrostatics simulations (see Methods). We consider two cases: incident light polarized along the long axis, Figure 6A, and incident light polarized along the short axis, Figure 6B, of the nanoparticle. For each case, we obtain the optical force components normal to the glass surface ( $z$  direction in Figure 6) and parallel to the propagating direction of the evanescent wave ( $x$  direction in Figure 6). These normal and parallel force components can be roughly thought of as gradient and radiation pressure forces, respectively, although it is important to note that they are obtained with a full electrostatics formalism and so are not exactly these simpler forces. To complement these calculations, we also adapted the TIR-induced optical force model of Arias-Gonzalez and Nieto-Vesperinas,<sup>58</sup> approximating the bipyramidal particles as prolate ellipsoids that are of the same volume and give a long-axis resonance near 810 nm in water (see Supporting Information). In this model, the parallel force is proportional to the imaginary part of the polarizability, i.e., the absorbance, and the normal force is proportional to the real part of the polarizability.

The FDTD results are given in panels C and D of Figure 6 for the case of the bipyramid (center) being at a distance of 30 nm (center to interface) from the interface. The optical forces are markedly different depending on the orientation of the nanoparticle relative to the incident polarization. For the case of polarization parallel to the nanoparticle's long axis (Figure 6C), the parallel force is always positive (i.e. repulsive) and peaks near 850 nm with a magnitude of  $\sim 0.5$  pN. This behavior is qualitatively consistent with the simple model discussed in the Supporting Information. In pure water and plane wave illumination, the FDTD absorption has a maximum at  $\approx 820$  nm, and so the maximum in the parallel force for TIR illumination is just slightly to the red of the absorbance maximum in pure water. The proximity to the glass surface shifts the bipyramid absorbance to the red owing to the higher index of glass. On the other hand, for electric field polarization perpendicular to the bipyramid's long axis, Figure 6D, the parallel force effectively goes to zero. This is because the effective absorbance is now dominated by the bipyramid's short axis and is significant only at much shorter wavelengths.

The normal force shows different behavior in the wavelength range of interest. From Figure 6C we see that when light is

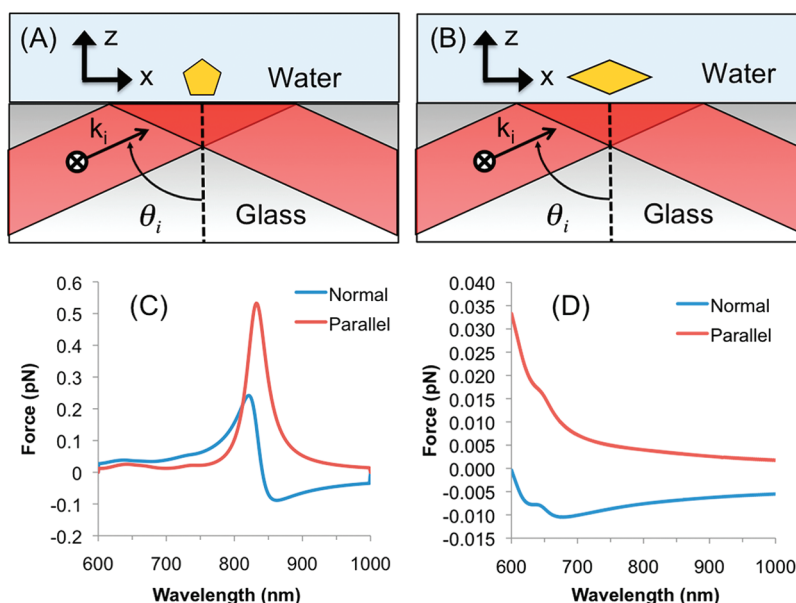


**Figure 6.** Schematic of FDTD simulation geometries for Au bipyramid long axis oriented (A) parallel and (B) perpendicular to laser polarization. The angle of incidence  $\theta_i$  and incident wave vector  $k_i$  are noted. The polarization direction is perpendicular to the page. (C, D) Force spectra for parallel and perpendicular orientations, respectively. Note that negative values of the force mean attraction to the surface.

polarized along the long bipyramid axis, the normal force is positive (i.e., repulsive) for  $\lambda < 835$  nm and negative (i.e., attractive) for  $\lambda > 835$  nm. Again, this behavior is qualitatively consistent with the simple model (Supporting Information). Furthermore the forces from FDTD and the analytical model are comparable.

The magnitude of the parallel force for the case of polarization parallel to the bipyramidal long axis (Figure 6A) is significantly larger than the experimental estimate based on a steady-state solution of the viscous drag force from a Langevin equation, as given above. There are several possible reasons for this. First, the bipyramids in solution will be tumbling due to thermal motions and thus will experience a time-varying optical force as their long axis comes into and out of alignment with the laser polarization.<sup>34</sup> It should be noted as well that even when the bipyramid is perpendicular to the laser polarization, it should still experience a nonzero normal or gradient force driving it toward the surface; see Figure 6D which shows negative (i.e., attractive) normal force for all wavelengths of interest. These forces are significantly lower in magnitude relative to the aligned case. Another reason for the discrepancy can be explained by the nature of the photothermal annealing process. Rapid heating of the bipyramids will likely take place within 10s of nanoseconds of their exposure to the laser beam.<sup>59,60</sup> Afterward, photothermal annealing will reduce the bipyramids' aspect ratio and thus cause a blue-shift in their longitudinal plasmon resonance peaks. As shown in Figure 6C, a blue-shift of the longitudinal plasmon resonance relative to the trapping laser wavelength will (a) reduce the parallel or scattering force and (b) enhance the normal or gradient force toward the surface, assuming that the annealed bipyramid's peak is now blue of the laser line.

The actual temperature rise occurring at the bipyramids' surfaces as they deposit is difficult to access experimentally, although a few techniques have been recently developed, e.g., utilizing fluorescence anisotropy or vesicle cargo release.<sup>61,62</sup> Several theoretical models have been developed to describe the

temperature increase of spherical Au nanoparticles exposed to either continuous or pulsed laser excitation.<sup>59,60,63–65</sup> The release of heat from optically excited Au nanoparticles can take place by radiation, convection, and conduction, with the latter two mechanisms expected to take precedence over the former for the case of Au nanoparticles dissolved in water.<sup>60</sup>

Since the details of convective heat transfer from nanoparticles are at present poorly understood<sup>66</sup> and are the subject of current research, we will make an upper limit estimate of the nanoparticle surface temperature ignoring convective and radiative heat transport (see Supporting Information for details of the calculation method). In the range of radial distances at which bipyramids are observed to deposit,  $r \sim 1–3 \mu\text{m}$ , the rise of the surface temperature of the nanoparticle above room temperature  $\Delta T$  at the glass surface ( $z = 0$ ) is large,  $\sim 300$  K. However, farther from the surface  $\Delta T$  is smaller due to the diminished evanescent field magnitude, reaching a maximum of 205 K for  $z = 200$  nm. These calculations show that significant thermal energy can be absorbed by the bipyramids from the optical field intensities present in the experiment. However, thermally induced annealing, which has been reported to take place at temperatures as low as 60 °C in Au nanorods,<sup>67</sup> would likely occur before the previously mentioned values of  $\Delta T$  are reached. Furthermore, any shape change of the Au bipyramids will shift their resonance away from the trapping laser; thus the optical heating is self-limiting.

We have considered many possible explanations of the observations. However, the totality of the experimental and simulation results suggest a two-part mechanism for the deposition of Au bipyramids. First, radiation pressure and the gradient force act to transport the bipyramids toward the surface. Next, photothermal heating causes a loss of stability of the bipyramids' ligand coating, allowing them to deposit irreversibly on the glass surface. Thus, bipyramid deposition will only take place when the induced photothermal heating is sufficient to overcome the energy barrier for the dissociation of the ligand coating (cetyl trimethylammonium bromide, CTAB). This reasoning could

account for the “threshold” behavior of the power-dependent deposition rate  $R(P)$ , although the threshold could also be the result of the optical potential being smaller than  $1/2k_B T$ . At optical powers greater than that necessary for CTAB dissociation, the linear behavior of  $R(P)$  is most likely due to the greater flux of bipyramids into the evanescent field area due to the increased scattering force.

The observed crescent-shaped deposition pattern is a result of the optical forces acting of the Au bipyramids in solution. The optical force vector contains components both normal and parallel to the surface. Particles (i.e., bipyramids) that are resonant with the laser light entering the evanescent field area from upstream of the scattering-induced flow experience an increasing electrodynamic (plasmonic) force that accelerates them toward the surface, where they deposit. On the other hand, particles entering the evanescent field area from any other direction are pushed to a region of lower optical intensity by the scattering force, which can be significantly larger than the gradient force. The result is that particles deposit only near the periphery of the illuminated area that is upstream from the scattering-induced flow, forming the observed crescent shape on the surface.

The role of a threshold for bipyramid deposition is apparent in the power-dependent pattern formation shown in Figure 4. At lower powers the bipyramids' surface temperatures increase sufficiently to cause deposition only near the center of the evanescent field area. On the other hand, in the high-power limit, the bipyramids deposit rapidly; for our measurement time resolution (30 ms), as soon as they come in contact with the evanescent field. The acceleration and directional motion leads to deposition at the perimeter of the evanescent field area, as previously mentioned. At the lowest optical power tested in Figure 4, 40 mW, the deposited bipyramids appear clustered near the center of the evanescent field spot. This combined with  $R(P)$  in Figure 3B indicates that for the experimental parameters given 40 mW is a threshold power for deposition.

In conclusion, we have shown in experiments that near-IR laser light undergoing TIR at a glass–water interface can be used to controllably deposit bipyramidal Au nanoparticles on transparent (i.e., glass) surfaces. Together with FDTD simulations and from analytical model calculations of the optical forces, we conclude that the process is plasmon resonance selective. A clear corroboration is the selective (even exclusive) deposition of Au bipyramids versus nonresonant spheroidal Au nanoparticles. Combined with the highly wavelength-dependent deposition rate, this shows that the deposition is due to resonant absorption of the bipyramids. The deposition mechanism involves driven particle motion, as elucidated from experimental results and from electrodynamic simulations of the optical forces on the particles, with a significant gradient force toward the surface and resonant heating of the bipyramids. The latter causes a loss of colloidal stability that allows irreversible binding to the glass surface. Model calculations show that there is more than sufficient heat to promote thermal annealing of the bipyramids upon resonant absorption of the evanescent optical field. Direct correlation of the dark-field spectra of deposited bipyramids with structural data obtained by SEM reveals a wavelength-dependent reduction in aspect ratio, further confirming the proposed photothermal annealing.

The results presented herein have several important ramifications. To our knowledge this is the first demonstration of the plasmon-selective deposition of metal nanoparticles, a discovery that could accelerate the development of devices such as multiplex biosensor arrays based on these particles. In particular,

considering the difficulty of synthesizing high aspect ratio Ag nanoparticles (such as rods and wires) with well-controlled lengths, TIR trapping could be used to deposit only particles with the desired plasmon resonance peak from a heterogeneous mixture of nanoparticle shapes. More generally, TIR trapping could be used to pattern the same surface with a wide variety of different types of plasmonic metal nanoparticles, varying by composition, shape, size, dielectric coating, state of aggregation, or any other variable that alters the plasmon absorption peak in the near-IR. Deposition patterns of controlled shape should be obtainable with actively steered beams while standing wave excitation should eliminate the driven motion parallel to the surface. Finally, although the results from the current experiment show some orientational order, the opposing orientational tendencies of the scattering and gradient forces need to be eliminated. Illumination with structured optical beams should allow gaining the desired control.

Furthermore, this work illustrates the important consideration of photothermal annealing of high-aspect ratio metal nanostructures for both fundamental and applied plasmonic research. For example, for applications that rely on the local heating generated by metal nanoparticles such as photothermal cancer therapy,<sup>68</sup> annealing will shift the plasmon off resonance with the exciting field, limiting the effectiveness of the therapy. Similarly, the potential use of high-aspect ratio metal nanoparticles for photothermal catalysis<sup>69</sup> could encounter the same problem. Coating the Au bipyramids with a layer of silica could prevent thermal annealing by locking the structure.<sup>70</sup>

**Methods.** *Materials.* Au bipyramids were synthesized according to literature protocols.<sup>55</sup> Excess CTAB was removed by centrifugation and resuspension in a manner similar to what has been previously described.<sup>6</sup> Briefly, the excess CTAB in solution after synthesis was allowed to precipitate either at room temperature overnight or at 4 °C for a few hours. The remaining solution was then decanted and centrifuged at 9500 rpm for 10 min. The precipitate was resuspended in 18 M $\Omega$  resistivity water.

Number 1.5 glass coverslips ( $\sim 170 \mu\text{m}$  thickness) were used as received from Corning. A clean silicone gasket was sandwiched between two coverslips to form the sample cell. This formed a watertight seal between the silicone and the glass surface and allowed for easy disassembly of the sample cell after the experiment. After the deposition was performed, the coverslip was then washed thoroughly with 18 M $\Omega$  water in order to prevent any particle left in solution from depositing, dried using compressed air, and stored under vacuum until imaged. Following TIR trapping/deposition, the coverslips were sputtered with a thin ( $\sim 4 \text{ nm}$ ) layer of Pt/Pd to prevent charging during SEM imaging. The washing procedure did not appear to remove any particles that had been deposited, as judged from the fact that the same crescent patterns observed in the optical experiment were reproduced under SEM imaging.

*FDTD Simulations.* Three-dimensional FDTD simulations<sup>57</sup> are performed with the commercial code FDTD Solutions (Vancouver, Canada). We consider a gold bipyramid (84 nm long, and maximum pentagonal radius 15 nm) in water (refractive index 1.33) above a glass substrate (refractive index 1.5). An auxiliary differential equations model that closely fits the Johnson-Christy complex, dispersive refractive index data for gold<sup>71</sup> is used and the long axis of the nanoparticle is parallel to the glass surface. In these calculations, a time-windowed plane wave from the glass side (s-polarized), with incident angle  $\theta_i = 70^\circ$  relative to the surface normal is used to generate evanescent

waves emanating from the glass/water interface and extending into the water. The incident field is actually spectrally broadband as obtained from a short (few fs) duration pulse. We orient the nanoparticle such that either its long axis or its short axis is aligned with the incident polarization direction; see, e.g., panels A and B of Figure 6. The optical forces are obtained from the electric and magnetic fields by integrating the Maxwell stress tensor across a closed surface containing a bipramid.<sup>49,72</sup> This analysis is performed so as to reveal the wavelength dependence of the force.

**Laser System and Imaging.** The laser system employed is a home-built wavelength-tunable (740–840 nm) continuous-wave (CW) Ti:sapphire pumped by a 5 W capable Nd:YVO laser (Millenia; Spectra Physics). After spatial filtering with a 50  $\mu\text{m}$  diamond pinhole, the beam was focused onto the edge of the back aperture of a 100 $\times$  oil immersion objective lens (Olympus UPLSAPO). A reflective neutral density filter (Edmund Optical) mounted in an Olympus IX71 inverted microscope was used to reflect  $\sim 50\%$  of the beam power into the microscope objective. The laser polarization was “S” with respect to the coverslip surface (electric field in the plane of the coverslip).

Au bipyramid deposition on the coverslip surface was observed by blocking the internally reflected beam immediately after its exit from the back aperture of the objective lens. This configuration allowed for any scattering (from a nanoparticle) within the evanescent field volume to be imaged onto a Watec 902B CCD camera. The size of the evanescent field area was measured via collecting several images of scattering from non-specifically (i.e., randomly) deposited metal nanoparticles and summing the images together using image processing software (ImageJ). The resulting image reflects the spatial profile of the evanescent field. The central part of this image was integrated about the azimuthal angle to determine its radial profile, which was fitted to a Gaussian function with a full width at half-maximum (fwhm) of 5.7  $\mu\text{m}$ .

The total power delivered to the sample was estimated based on the manufacturer’s specification for transmission at 800 nm ( $\sim 70\%$ ) and the optical power measured entering the microscope objective.

## ■ ASSOCIATED CONTENT

**S Supporting Information.** Results of experiments in  $\text{D}_2\text{O}$ , calculation of conductive heating of Au nanoparticles, Figures S1 and S2 and a movie depicting TIR-based Au bipyramid deposition, and details and results of the model optical force calculations, Figure S3. This material is available free of charge via the Internet at <http://pubs.acs.org>

## ■ AUTHOR INFORMATION

### Corresponding Author

\*E-mail: [nfschere@uchicago.edu](mailto:nfschere@uchicago.edu).

## ■ ACKNOWLEDGMENT

We thank Dr. Matt Pelton, Professor Phillippe Guyot-Sionnest and Professor Tom Witten for useful discussions. We thank Dr. Lina Cao for performing preliminary FDTD simulations for this paper. This work was supported in part by the National Science Foundation (CHE-0616663) and the Dreyfus Foundation Postdoctoral Program in Environmental Chemistry. Additional support was obtained from the Chemical Sciences, Geosciences, and

Biosciences Division of the Office of Basic Energy Sciences, Office of Science, U.S. Department of Energy (from a SISGR grant) under Contract Number DE-AC02-06CH11357. Use of the Center for Nanoscale Materials at Argonne National Laboratory was supported by U.S. Department of Energy, Office of Science, Office of Basic Energy Sciences, under Contract No. DE-AC02-06CH11357. We thank Dr. Qiti Guo for assistance with the use of central facilities of the NSF-Materials Research Science and Engineering Center (MRSEC; no. 0820054).

## ■ REFERENCES

- (1) Pelton, M.; Aizpurua, J.; Bryant, G. Metal-nanoparticle plasmonics. *Laser Photonics Rev.* **2008**, *2* (3), 136–159.
- (2) Schuller, J. A.; Barnard, E. S.; Cai, W.; Jun, Y. C.; White, J. S.; Brongersma, M. L. Plasmonics for extreme light concentration and manipulation. *Nat. Mater.* **2010**, *9* (3), 193–204.
- (3) Anker, J. N.; Hall, W. P.; Lyandres, O.; Shah, N. C.; Zhao, J.; Van Duyne, R. P. Biosensing with plasmonic nanosensors. *Nat. Mater.* **2008**, *7* (6), 442–453.
- (4) Falk, A. L.; Koppens, F. H. L.; Yu, C. L.; Kang, K.; de Leon Snapp, N.; Akimov, A. V.; Jo, M. H.; Lukin, M. D.; Park, H. Near-field electrical detection of optical plasmons and single-plasmon sources. *Nat. Phys.* **2009**, *5*, 475–479.
- (5) Catchpole, K. R.; Polman, A. Plasmonic solar cells. *Opt. Express* **2008**, *16* (26), 21793–21800.
- (6) Burgin, J.; Liu, M. Z.; Guyot-Sionnest, P. Dielectric Sensing with Deposited Gold Bipyramids. *J. Phys. Chem. C* **2008**, *112* (49), 19279–19282.
- (7) Lee, S.; Mayer, K. M.; Hafner, J. H. Improved localized surface plasmon resonance immunoassay with gold bipyramid substrates. *Anal. Chem.* **2009**, *81* (11), 4450–4455.
- (8) Mayer, K. M.; Hao, F.; Lee, S.; Nordlander, P.; Hafner, J. H. A single molecule immunoassay by localized surface plasmon resonance. *Nanotechnology* **2010**, *21* (25), 8.
- (9) Romero, I.; Aizpurua, J.; Bryant, G. W.; de Abajo, F. J. G. Plasmons in nearly touching metallic nanoparticles: singular response in the limit of touching dimers. *Opt. Express* **2006**, *14* (21), 9988–9999.
- (10) Zuloaga, J.; Prodan, E.; Nordlander, P. Quantum Plasmonics: Optical Properties and Tunability of Metallic Nanorods. *ACS Nano* **2010**, *4*, 5269–5276.
- (11) Haynes, C. L.; McFarland, A. D.; Zhao, L. L.; Van Duyne, R. P.; Schatz, G. C.; Gunnarsson, L.; Prikulis, J.; Kasemo, B.; Kall, M. Nanoparticle optics: The importance of radiative dipole coupling in two-dimensional nanoparticle arrays. *J. Phys. Chem. B* **2003**, *107*, 7337–7342.
- (12) Dittlacher, H.; Hohenau, A.; Wagner, D.; Kreibitz, U.; Rogers, M.; Hofer, F.; Aussenegg, F. R.; Krenn, J. R. Silver nanowires as surface plasmon resonators. *Phys. Rev. Lett.* **2005**, *95* (25), 257403–257403.
- (13) Huang, W.; Qian, W.; El-Sayed, M. A.; Ding, Y.; Wang, Z. L. Effect of the Lattice Crystallinity on the Electron–Phonon Relaxation Rates in Gold Nanoparticles. *J. Phys. Chem. C* **2007**, *111* (29), 10751–10757.
- (14) Chen, K. P.; Drachev, V. P.; Borneman, J. D.; Kildishev, A. V.; Shalaev, V. M. Drude Relaxation Rate in Grained Gold Nanoantennas. *Nano Lett.* **2010**, *10*, 916–922.
- (15) Heath, J. R.; Knobler, C. M.; Leff, D. V. Pressure/temperature phase diagrams and superlattices of organically functionalized metal nanocrystal monolayers: The influence of particle size, size distribution, and surface passivant. *J. Phys. Chem. B* **1997**, *101* (2), 189–197.
- (16) Lin, X. M.; Jaeger, H. M.; Sorensen, C. M.; Klabunde, K. J. Formation of long-range-ordered nanocrystal superlattices on silicon nitride substrates. *J. Phys. Chem. B* **2001**, *105* (17), 3353–3357.
- (17) Tao, A.; Sinsersuksakul, P.; Yang, P. Tunable plasmonic lattices of silver nanocrystals. *Nat. Nanotechnol.* **2007**, *2* (7), 435–440.
- (18) Shevchenko, E. V.; Talapin, D. V.; Kotov, N. A.; O’Brien, S.; Murray, C. B. Structural diversity in binary nanoparticle superlattices. *Nature* **2006**, *439*, 55–59.

- (19) Huang, Y.; Duan, X.; Wei, Q.; Lieber, C. M. Directed assembly of one-dimensional nanostructures into functional networks. *Science* **2001**, *291* (5504), 630.
- (20) Koh, S. J. Strategies for controlled placement of nanoscale building blocks. *Nanoscale Res. Lett.* **2007**, *2* (11), 519–545.
- (21) Cui, Y.; Bjork, M. T.; Liddle, J. A.; Sonnichsen, C.; Boussett, B.; Alivisatos, A. P. Integration of colloidal nanocrystals into lithographically patterned devices. *Nano Lett.* **2004**, *4* (6), 1093–1098.
- (22) Kraus, T.; Malaquin, L.; Schmid, H.; Riess, W.; Spencer, N. D.; Wolf, H. Nanoparticle printing with single-particle resolution. *Nat. Nanotechnol.* **2007**, *2* (9), 570–576.
- (23) Cohen, A. E. Control of nanoparticles with arbitrary two-dimensional force fields. *Phys. Rev. Lett.* **2005**, *94* (11), 118102.
- (24) Ma, L. C.; Subramanian, R.; Huang, H. W.; Ray, V.; Kim, C. U.; Koh, S. J. Electrostatic funneling for precise nanoparticle placement: a route to wafer-scale integration. *Nano Lett.* **2007**, *7* (2), 439–445.
- (25) Jamshidi, A.; Neale, S. L.; Yu, K.; Pauzaskie, P. J.; Schuck, P. J.; Valley, J. K.; Hsu, H.-Y.; Ohta, A. T.; Wu, M. C. NanoPen: Dynamic, Low-Power, and Light-Actuated Patterning of Nanoparticles. *Nano Lett.* **2009**, *9* (8), 2921–2925.
- (26) Demers, L. M.; Ginger, D. S.; Park, S. J.; Li, Z.; Chung, S. W.; Mirkin, C. A. Direct patterning of modified oligonucleotides on metals and insulators by dip-pen nanolithography. *Science* **2002**, *296* (5574), 1836–1838.
- (27) Salaita, K.; Wang, Y.; Mirkin, C. A. Applications of dip-pen nanolithography. *Nat. Nanotechnol.* **2007**, *2* (3), 145–155.
- (28) Svoboda, K.; Block, S. M. Optical Trapping of Metallic Rayleigh Particles. *Opt. Lett.* **1994**, *19* (13), 930–932.
- (29) Hansen, P. M.; Bhatia, V. K.; Harrit, N.; Oddershede, L. Expanding the optical trapping range of gold nanoparticles. *Nano Lett.* **2005**, *5* (10), 1937–1942.
- (30) Bosanac, L.; Aabo, T.; Bendix, P. M.; Oddershede, L. B. Efficient optical trapping and visualization of silver nanoparticles. *Nano Lett.* **2008**, *8* (5), 1486–1491.
- (31) Zhang, Y.; Gu, C.; Schwartzberg, A. M.; Chen, S.; Zhang, J. Z. Optical trapping and light-induced agglomeration of gold nanoparticle aggregates. *Phys. Rev. B* **2006**, *73* (16), 165405.
- (32) Jones, P. H.; Palmisano, F.; Bonaccorso, F.; Gucciardi, P. G.; Calogero, G.; Ferrari, A. C.; Maragó, O. M. Rotation Detection in Light-Driven Nanorotors. *ACS Nano* **2009**, *3* (10), 3077–3084.
- (33) Itoh, T.; Ozaki, Y.; Yoshikawa, H.; Ihama, T.; Masuhara, H., Hyper-Rayleigh scattering and hyper-Raman scattering of dye-adsorbed silver nanoparticles induced by a focused continuous-wave near-infrared laser. *Appl. Phys. Lett.* **2006**, *88* (Journal Article).
- (34) Pelton, M.; Liu, M. Z.; Kim, H. Y.; Smith, G.; Guyot-Sionnest, P.; Scherer, N. F. Optical trapping and alignment of single gold nanorods by using plasmon resonances. *Opt. Lett.* **2006**, *31* (13), 2075–2077.
- (35) Selhuber-Unkel, C.; Zins, I.; Schubert, O.; Sonnichsen, C.; Oddershede, L. B. Quantitative optical trapping of single gold nanorods. *Nano Lett.* **2008**, *8* (9), 2998–3003.
- (36) Toussaint, K. C.; Liu, M.; Pelton, M.; Pesic, J.; Guffey, M. J.; Guyot-Sionnest, P.; Scherer, N. F. Plasmon resonance-based optical trapping of single and multiple Au nanoparticles. *Opt. Express* **2007**, *15* (19), 12017–12029.
- (37) Tong, L.; Miljkovic, V. D.; Kall, M. Alignment, rotation, and spinning of single plasmonic nanoparticles and nanowires using polarization dependent optical forces. *Nano Lett.* **2010**, *10* (1), 268–273.
- (38) Guffey, M. J.; Scherer, N. F. All-Optical Patterning of Au Nanoparticles on Surfaces Using Optical Traps. *Nano Lett.* **2010**, *10* (11), 4302–4308.
- (39) Kawata, S.; Sugiura, T. Movement of Micrometer-Sized Particles in the Evanescent Field of a Laser-Beam. *Opt. Lett.* **1992**, *17* (11), 772–774.
- (40) Kawata, S.; Tani, T. Optically driven Mie particles in an evanescent field along a channeled waveguide. *Opt. Lett.* **1996**, *21* (21), 1768–1770.
- (41) Sasaki, K.; Hotta, J. I.; Wada, K.; Masuhara, H. Analysis of radiation pressure exerted on a metallic particle within an evanescent field. *Opt. Lett.* **2000**, *25* (18), 1385–1387.
- (42) Garces-Chavez, V.; Dholakia, K.; Spalding, G. C. Extended-area optically induced organization of microparticles on a surface. *Appl. Phys. Lett.* **2005**, *86* (3), 031106.
- (43) Wang, K.; Schonbrun, E.; Crozier, K. B. Propulsion of Gold Nanoparticles with Surface Plasmon Polaritons: Evidence of Enhanced Optical Force from Near-Field Coupling between Gold Particle and Gold Film. *Nano Lett.* **2009**, *9* (7), 2623–2629.
- (44) Nie, S. M.; Emery, S. R. Probing single molecules and single nanoparticles by surface-enhanced Raman scattering. *Science* **1997**, *275* (5303), 1102–1106.
- (45) Jin, R.; Jureller, J. E.; Kim, H. Y.; Scherer, N. F. Correlating second harmonic optical responses of single Ag nanoparticles with morphology. *J. Am. Chem. Soc.* **2005**, *127* (36), 12482–12483.
- (46) Jin, R.; Jureller, J. E.; Scherer, N. F. Precise localization and correlation of single nanoparticle optical responses and morphology. *Appl. Phys. Lett.* **2006**, *88* (26), 263111–263111.
- (47) Beversluis, M. R.; Bouhelier, A.; Novotny, L. Continuum generation from single gold nanostructures through near-field mediated interband transitions. *Phys. Rev. B* **2003**, *68* (11), 115433–115433.
- (48) Quidant, R.; Petrov, D.; Badenes, G. Radiation forces on a Rayleigh dielectric sphere in a patterned optical near field. *Opt. Lett.* **2005**, *30* (9), 1009–1011.
- (49) Nome, R. A.; Guffey, M. J.; Scherer, N. F.; Gray, S. K. Plasmonic interactions and optical forces between two bipyramidal nanoparticle dimers. *J. Phys. Chem. A* **2009**, *113* (16), 4408–4415.
- (50) Righini, M.; Zelenina, A. S.; Girard, C.; Quidant, R. Parallel and selective trapping in a patterned plasmonic landscape. *Nat. Phys.* **2007**, *3* (7), 477–480.
- (51) Righini, M.; Volpe, G.; Girard, C.; Petrov, D.; Quidant, R. Surface plasmon optical tweezers: tunable optical manipulation in the femtonewton range. *Phys. Rev. Lett.* **2008**, *100* (18), 186804.
- (52) Righini, M.; Ghenuche, P.; Cherukulappurath, S.; Myroshnychenko, V.; Garcia de Abajo, F. J.; Quidant, R. Nano-optical trapping of Rayleigh particles and Escherichia coli bacteria with resonant optical antennas. *Nano Lett.* **2009**, *9* (10), 3387–3391.
- (53) Braun, C. L.; Smirnov, S. N. Why is water blue? *J. Chem. Educ.* **1993**, *70* (8), 612.
- (54) Kou, L.; Labrie, D.; Chylek, P. Refractive indices of water and ice in the 0.65- to 2.5- $\mu\text{m}$  spectral range. *Appl. Opt.* **1993**, *32* (19), 3531–3540.
- (55) Liu, M. Z.; Guyot-Sionnest, P. Mechanism of silver(I)-assisted growth of gold nanorods and bipyramids. *J. Phys. Chem. B* **2005**, *109* (47), 22192–22200.
- (56) Hoogeveen, R. W. M.; Spreuw, R. J. C.; Hermans, L. J. F. Observation of surface light-induced drift. *Phys. Rev. Lett.* **1987**, *59* (4), 447.
- (57) Taflove, A.; Hagness, S. C. *Computational electrodynamics: the finite-difference time-domain method*; Artech House: Boston, MA, 2005.
- (58) Arias-González, J. R.; Nieto-Vesperinas, M. Optical forces on small particles: attractive and repulsive nature and plasmon-resonance conditions. *J. Opt. Soc. Am. A* **2003**, *20* (7), 1201–1209.
- (59) Pitsillides, C. M.; Joe, E. K.; Wei, X.; Anderson, R.; Lin, C. P. Selective cell targeting with light-absorbing microparticles and nanoparticles. *Biophys. J.* **2003**, *84* (6), 4023–4032.
- (60) Harris, N.; Ford, M. J.; Cortie, M. B. Optimization of plasmonic heating by gold nanospheres and nanoshells. *J. Phys. Chem. B* **2006**, *110* (22), 10701–10707.
- (61) Baffou, G.; Girard, C.; Quidant, R. Mapping Heat Origin in Plasmonic Structures. *Phys. Rev. Lett.* **2010**, *104*, 13.
- (62) Kyrsting, A.; Bendix, P. M.; Stamou, D. G.; Oddershede, L. B. Heat Profiling of Three-Dimensionally Optically Trapped Gold Nanoparticles using Vesicle Cargo Release. *Nano Lett.* **2010**, *11* (2), 888–892.
- (63) Pustovalov, V. K. Theoretical study of heating of spherical nanoparticle in media by short laser pulses. *Chem. Phys.* **2005**, *308* (1–2), 103–108.
- (64) Govorov, A. O.; Zhang, W.; Skeini, T.; Richardson, H.; Lee, J.; Kotov, N. A. Gold nanoparticle ensembles as heaters and actuators: melting and collective plasmon resonances. *Nanoscale Res. Lett.* **2006**, *1* (1), 84–90.

(65) Baffou, G.; Quidant, R.; García de Abajo, F. J. Nanoscale Control of Optical Heating in Complex Plasmonic Systems. *ACS Nano* **2010**, *4* (2), 709–716.

(66) Baffou, G.; Quidant, R.; Girard, C. Heat generation in plasmonic nanostructures: Influence of morphology. *Appl. Phys. Lett.* **2009**, *94* (15), 153109.

(67) Mohamed, M. B.; Ismail, K. Z.; Link, S.; El-Sayed, M. Thermal Reshaping of Gold Nanorods in Micelles. *J. Phys. Chem. B* **1998**, *102* (47), 9370–9374.

(68) Huang, X.; Jain, P.; El-Sayed, I.; El-Sayed, M. Plasmonic photothermal therapy (PPTT) using gold nanoparticles. *Lasers Med. Sci.* **2008**, *23* (3), 217–228.

(69) Adleman, J. R.; Boyd, D. A.; Goodwin, D. G.; Psaltis, D. Heterogenous Catalysis Mediated by Plasmon Heating. *Nano Lett.* **2009**, *9* (12), 4417–4423.

(70) Pastoriza-Santos, I.; Pérez-Juste, J.; Liz-Marzán, L. M. Silica-coating and hydrophobation of CTAB-stabilized gold nanorods. *Chem. Mater.* **2006**, *18* (10), 2465–2467.

(71) Johnson, P. B.; Christy, R. W. Optical-Constants of Noble-Metals. *Phys. Rev. B* **1972**, *6* (12), 4370–4379.

(72) Nieto-Vesperinas, M.; Chaumet, P. C.; Rahmani, A. Near-field photonic forces. *Philos. Trans. R. Soc., A* **2004**, *362*, 719–737.